Systems/Circuits

Cortical Control of Spatial Resolution by VIP$^+$ Interneurons

Inbal Ayzenshtat, Mahesh Miikael Karnani, Jesse Jackson, and Rafael Yuste
NeuroTechnology Center, Department of Biological Sciences, Columbia University, New York, New York 10027

Neuronal tuning, defined by the degree of selectivity to a specific stimulus, is a hallmark of cortical computation. Understanding the role of GABAergic interneurons in shaping cortical tuning is now possible with the ability to manipulate interneuron classes selectively. Here, we show that interneurons expressing vasoactive intestinal polypeptide (VIP$^+$) regulate the spatial frequency (SF) tuning of pyramidal neurons in mouse visual cortex. Using two-photon calcium imaging and optogenetic manipulations of VIP$^+$ cell activity, we found that activating VIP$^+$ cells elicited a stronger network response to stimuli of higher SFs, whereas suppressing VIP$^+$ cells resulted in a network response shift toward lower SFs. These results establish that cortical inhibition modulates the spatial resolution of visual processing and add further evidence demonstrating that feature selectivity depends, not only on the feedforward excitatory projections into the cortex, but also on dynamic intracortical modulations by specific forms of inhibition.

Key words: cortical tuning; inhibition; interneurons; spatial resolution; VIP+; visual cortex

Significance Statement

We demonstrate that interneurons expressing vasoactive intestinal polypeptide (VIP$^+$) play a causal role in regulating the spatial frequency (SF) tuning of neurons in mouse visual cortex. We show that optogenetic activation of VIP$^+$ cells results in a shift in network preference toward higher SFs, whereas suppressing them shifts the network toward lower SFs. Several studies have shown that VIP$^+$ cells are sensitive to neuromodulation and increase their firing during locomotion, whisking, and pupil dilation and are involved in spatially specific top-down modulation, reminiscent of the effects of top-down attention, and also that attention enhances spatial resolution. Our findings provide a bridge between these studies by establishing the inhibitory circuitry that regulates these fundamental modulations of SF in the cortex.

Introduction

The contribution of GABAergic interneurons to regulating thalamic inputs and shaping the basic properties of cortical pyramidal neurons has been demonstrated using coarse-grained pharmacological manipulations (Sillito, 1975, 1979; Kyriazi et al., 1996; Wang et al., 2000; Katzner et al., 2011) and more specific optogenetic manipulations of interneuron subpopulations. For example, parvalbumin-expressing (PV$^+$) cells linearly transform excitatory responses and preserve stimulus selectivity (Atallah et al., 2012; Wilson et al., 2012), whereas somatostatin-expressing (SOM$^+$) cells subtract responses and sharpen selectivity (Wilson et al., 2012; but see Lee et al., 2012, 2014) and contribute to surround suppression (Adesnik et al., 2012). These studies have demonstrated dissociable roles of distinct classes of interneurons in controlling the firing dynamics of pyramidal cells.

Here we focus on a third class of cortical interneurons, those expressing vasoactive intestinal polypeptide (VIP$^+$). VIP$^+$ cells exhibit distinct morphology and cortical laminar distribution (Xu et al., 2010; Prönneke et al., 2015) and are activated by input from cholinergic neurons in the basal forebrain (Alitto and Dan, 2010; Fu et al., 2014). VIP$^+$ cells increase their firing during locomotion (Fu et al., 2014), whisking (Lee et al., 2013), or pupil dilation (Reimer et al., 2014) and have a disinhibitory influence on pyramidal cells, primarily by inhibition of SOM$^+$ cells (Lee et al., 2013; Pi et al., 2013; Jackson et al., 2016; Karnani et al., 2016a).

During sensory processing, VIP$^+$ cells are known to exert a complex influence on neuronal responses. In the auditory cortex, activating VIP$^+$ cells suppressed short-delayed evoked responses and enhanced long-delayed responses (Pi et al., 2013). In visual cortex, VIP$^+$ cells modulate long range corticocortical projections and improve visual discriminability (Zhang et al., 2014). We showed recently that VIP$^+$ cells have a general role in medi-

Received June 15, 2016; revised Sept. 15, 2016; accepted Sept. 19, 2016.

Author contributions: I.A. and R.Y. designed research; I.A. and M.M.K. performed research; I.A., M.M.K., and J.J. analyzed data; I.A. and R.Y. wrote the paper.

This work was supported by the Marie Curie Foundation (International Outgoing Fellowship to I.A.), the Human Frontier Science Program (Long-Term Fellowship to M.M.K), the Canadian Institute for Health Research (to J.J.), the National Eye Institute–National Institutes of Health (Grants DP1EY024503 and R01EY011787), and the Defense Advanced Research Projects Agency (DARPA SIMPLEX Grant N66001-15-C-4032). This material is based upon work supported by, or in part by, the U.S. Army Research Laboratory and the U.S. Army Research Office under contract number W911NF-12-1-0594 (MURI). We thank Darcy Peterka, Julia Sable, Yeonsook Shin, Alexa Semonche, Kasra Manoocheri, and William Snider for technical support; Aaron Kerlin and Mark Andermann for help with the DOG curve fitting; and Robert Shapley and Guy Zurawel for advice, suggestions, and helpful discussions.

Correspondence should be addressed to Dr. Inbal Ayzenshtat, NeuroTechnology Center, Department of Biological Sciences, Columbia University, 550 W. 120th St., New York, NY 10027. E-mail: inbalayzen@gmail.com.

DOI:10.1523/JNEUROSCI.1920-16.2016

 0270-6474/16/3611498-12$15.00/0

ating high-activity states (Jackson et al., 2016), particularly within local cortical regions (~240 μm) (Karnani et al., 2016b). In addition, VIP$^+$ cells play a role in regulating visual acuity in an experience-dependent manner (Mardinly et al., 2016). However, it is still unclear how VIP$^+$ interneurons affect the feedforward information processing of pyramidal cells in the primary visual cortex (V1) and shape visual coding properties such as orientation or spatial frequency (SF) tuning to mediate changes in visual sensitivity or acuity.

Here, we used *in vivo* two-photon Ca^{2+} imaging combined with bidirectional optogenetic manipulations to study how VIP$^+$ cells control sensory-driven dynamics of pyramidal cell firing. We imaged hundreds of neurons and found that VIP$^+$ interneurons play an important role in V1 tuning by significantly altering the SF selectivity of neurons in layer 2/3 of V1. Activation of VIP$^+$ cells shifted the SF tuning curve of pyramidal cells toward higher spatial frequencies, whereas suppression of VIP$^+$ cells caused a shift of pyramidal cell tuning toward lower SFs. Direction tuning curves of pyramidal cells were also altered upon manipulation of VIP$^+$ cell activity, demonstrating a decrease in orientation selectivity and broader tuning. These changes could be explained by the dependence of orientation tuning on SF, as demonstrated previously in the visual cortex of primates and cats (Andrews and Pollen, 1979; Vidyasagar and Sigüenza, 1985; Webster and De Valois, 1985; Zhu et al., 2010).

The results presented here provide additional evidence that cortical inhibition is critical for maintaining and modulating feature selectivity of cells in layer 2/3. These data support the view that the receptive field of a neuron is a dynamic property and local intracortical inhibition plays an essential role in controlling cortical receptive fields, thereby shaping the cortical representations of the visual world.

Materials and Methods

Animals

Animal handling and experimentation were performed in accordance with the National Institutes of Health and Columbia University institutional animal care guidelines. Animals of both sexes were used and were housed in a temperature-controlled environment on a 12 h light/dark cycle. VIP-Cre or SOM-Cre mice (The Jackson Laboratory) at postnatal day 40 (P40)–P80 were crossed with LSL-tdTomato (Ai14 strain) to identify VIP$^+$ or SOM$^+$ cells, respectively. We used a total of 18 mice in *in vivo* experiments: five in C1V1 photostimulation experiments, five in archaerhodopsin from *Halorubrum* strain TP009 (ArchT) photostimulation experiments, and eight in control experiments.

Surgery 1: Viral injections

Three to 4 weeks before the experiments, mice were injected stereotactically (Kopf Instruments) with either AAV5-Flex-ArchT-GFP or AAV5-DIO-C1V1-YFP. All viruses were obtained from the University of North Carolina Vector Core. Mice were anesthetized with isoflurane and a small craniotomy (0.1 × 0.1 mm) was made to insert a beveled injection needle (World Precision Instruments) at 2.5 mm lateral and 0.05 mm anterior to lambda. The needle was slowly lowered to 150–200 μm below the pial surface and virus was injected (500–1000 nl at a rate of 80 nl/min) using a UMP3 microsyringe pump (World Precision Instruments). The needle was left in place for an additional 5–10 min to allow viral diffusion. After removing the injection needle, the scalp was sutured and animals were given carprofen (5 mg/kg) to aid recovery.

Surgery 2: In vivo *experiments*

Three weeks or more after virus injection, the mice were placed on a warming plate (37°C) and anesthetized with isoflurane (initially 2% and reduced to 1–1.5% during surgery) administered via nose cone (Kopf Instruments). A custom-made titanium head-plate was attached to the skull using dental cement over the location of the virus injection. Subsequently, a craniotomy (~1 × 1 mm) was made over V1 (3.5–4.5 mm posterior to bregma, 2.3–2.7 mm lateral to midline; putative monocular region) using a dental drill (Osada). An ophthalmic ointment was applied to the eyes to prevent drying during surgery (and was later removed before imaging). For awake experiments, the animals were allowed to recover for 2–3 d after head-plate attachment and underwent habituation on a circular running disk with their head fixed for 1–3 h each day for 2–3 d and then a craniotomy was performed on the day of the imaging according to the above procedure.

Dye loading

For bulk loading of cortical neurons, Oregon Green Bapta-1 AM (OGB-1 AM; Invitrogen) was first mixed with 4 μl of pluronic acid (20% in DMSO) and further diluted in 35 μl of dye buffer (150 mM NaCl, 2.5 mM KCl, and 10 mM HEPES, pH 7.4). Then, 50 μM sulforhodamine-101 (SR101; Invitrogen) was added to the solution to label astrocytes (Nimmerjahn et al., 2004). Animals were head fixed and the dye was slowly pressure injected into the left visual cortex at a depth of ~130–200 μm below the dura surface (layer 2/3) at an angle of 30° with a micropipette (tip opening 1–2 μm) using Picospritzer II (2–4 injections, 10 psi, 8 min each) under visual control of two-photon imaging [10× water-immersion objective, 0.5 numerical aperture (NA) Olympus, 850 nm excitation]. Then, the exposed cortex was covered with agarose (1.5–2%; Sigma-Aldrich) and a cover glass (World Precision Instruments) to reduce brain motion. Data collection began 30–90 min after the injections to ensure dye uptake across a large number of cells. During data collection, light anesthesia was maintained with isoflurane (0.8–0.9%) administered via nose cone (Kopf Instruments). Heart rate, respiration, and oxygen saturation were monitored throughout the experiments using MouseOx (Starr Life Sciences) and the respiration rate was used to monitor and control anesthesia levels.

Two-photon Ca^{2+} imaging

Imaging was performed with a two-photon Moveable Objective Microscope (Sutter Instruments) and a mode-locked dispersion-precompensated Ti:sapphire laser (Chameleon Vision II; Coherent Technologies) as described previously (Miller et al., 2014). Frames were scanned through a 20× (0.95 NA; Olympus) or 25× (1.05 NA; Olympus) water-immersion objective. Laser intensity was controlled with a pockels cell (Conoptics) and ranged between 20 and 70 mW. Scanning and image acquisition were controlled using Mscan (4.07 frames/s for 512 × 512 pixels or 6.05 frames/s for 420 × 420 pixels; Sutter Instrument). OGB-1 and tdTomato fluorescence were excited at 950 or 1040 nm, respectively. Fluorescence changes collected with a 20× objective typically varied between 5% and 50% and between 10% and 70% with a 25× objective. Emission was collected using green (535/50 nm) and red (610/75 nm) filters (Chroma) simultaneously on two photomultiplier tubes (PMTs). During experiments combined with photostimulation, we collected only the green channel and used a 510/40 green filter to avoid PMT saturation. The use of this filter decreased the overall light collection and resulted in fluorescence changes of ~5–30%.

In awake experiments, animals were placed on a circular running disk. Locomotion tracking was performed using an optical computer mouse placed under the running disk. Locomotion was defined as occurring when the mouse moved >1 cm/s. In awake experiments, trials during locomotion were excluded from further analysis (5–15% of the total number of trials).

Visual stimulation

Visual stimuli were generated in MATLAB (RRID:SCR_001622; The MathWorks) using the Psychophysics toolbox (Brainard, 1997; Pelli, 1997; Kleiner et al., 2007) and displayed on a gamma-corrected LCD monitor (19 inches, 60 Hz refresh rate; Dell) positioned 15 cm from the contralateral eye, approximately 45° to the long axis of the animal (spanning ~114° vertical by ~140° horizontal of visual space). The presentation of the visual stimuli was synchronized with image acquisition using Mscan (Sutter Instrument) and a routine written in MATLAB such that each stimulus presentation was triggered on the beginning of frame acquisition. The actual time of stimulus presentation was detected with a silicon photodiode (Hamamatsu) attached to the bottom right corner of the screen.

We presented full-field square-wave drifting gratings (100% contrast, ~114°×140°) for 420 ms, followed by 3–5 s of uniform gray background (the mean luminance of the gratings) plus a blank condition. Grating orientation was perpendicular to the drift direction. Gratings were presented at 12 directions of motion in 30° steps, 3 sets of 4 spatial frequencies: [0.02, 0.03, 0.04, 0.06 cycles per degree (cpd)] or [0.01 0.02 0.04 0.06 cpd] or [0.01 0.02 0.04 0.08 cpd], and a temporal frequency (TF) of 1.5 Hz. All stimuli were block randomized and repeated 5–10 times and initial phase of the drifting gratings kept constant across all trials. Stimuli were presented in a pseudorandom order (with and without photostimulation), but time courses are shown after sorting (see Figs. 1*E*, 5*B*). In a separate set of experiments, we chose one SF and one TF (0.04 cpd, 1.5 Hz) and varied the stimulus presentation time (400, 1000, 2000 ms; see example in Fig. 1*D*).

We conducted most of our experiments using short presentation of drifting gratings (<1 s). Our rationale was as follows. First, short stimuli enabled two-photon Ca^{2+} imaging coupled with photostimulation. In the case of C1V1, using short stimuli restricted the light artifact to only two imaging frames, so we could quantify the evoked responses after stimulus presentation free of light contamination. In the case of suppression experiments using ArchT, it was crucial to avoid rebound firing, so we had to use long photostimulation and short visual stimulation to avoid the rebound spikes. Second, to assess tuning curves using short stimuli, we compared tuning curves of various stimulus durations (400, 1000, and 2000 ms). Even though short stimuli (<1 s) elicited responses in ~15% fewer cells than long stimuli (≥1 s), it improved the response reliability and the tuning sharpness of the cells (data not shown) and we were able to measure reliable responses from hundreds of cells per FOV. Third, previous studies used brief presentation of stationary stimuli such as sparse noise (Smith and Häusser, 2010), natural images (Ko et al., 2011), or bright/dark squares (Liu et al., 2009) and characterized the RF properties of cells robustly in V1 of mice. An additional study showed a high correlation between the orientation preference obtained by presenting Gaussian noise movies at 30 frames/s and the orientation preference obtained by presenting drifting gratings for 1.5 s (Niell and Stryker, 2008). Finally, there is evidence that a brief visual stimulus (<0.5 s) is sufficient to generate robust survival behaviors (Yilmaz and Meister, 2013), so presenting short stimuli is physiologically relevant to the animal behavior.

Photostimulation in vivo

To activate C1V1 or ArchT, we used a fiber-coupled LED (center wavelength 590 or 617 nm, respectively) with an LED driver (LEDD1B; Thorlabs). The fiber was coupled to a cannula (0.39 NA; Thorlabs) mounted on a micromanipulator and positioned adjacent to the edge of the craniotomy. Control of LED pulses and synchronization with visual stimulus were done using Session-Based Interface and Data Acquisition Toolbox in MATLAB, USB-6001 DAQ (National Instruments), and a MASTER-8 stimulator, such that the computer that controlled the Psychophysics toolbox received analog input triggers for every acquired frame and accordingly sent analog output triggers to the visual stimulus monitor and to the MASTER-8 stimulator that controlled the LED pulse train (see Fig. 2*F*). This ensured that the onset of LED pulse train and the onset of visual stimulus occurred less than ±16.66 ms apart (the refresh rate of the monitor was 60 Hz). The synchronization procedure was tested after experiments by inspecting the recorded analog triggers and the photodiode signal that was attached to the monitor.

To activate C1V1, LED light was delivered at each alternate trial for 420 ms in 33 Hz pulses lasting 10 ms. To activate ArchT, LED light was delivered at each alternate trial for 1.4 s continuously. LEDs were driven at maximal current output from the LED driver (light intensity: ~5–10 mW/mm^2). To block stray light, we used a custom-made black fabric cover wrapped around the objective and the optic fiber.

Data analysis

Image analysis. Data analysis was performed using built-in and custom-built software in MATLAB. Images were first converted to TIFF format and registered to correct for *x*–*y* motion using Turboreg plug-in in ImageJ (Thévenaz et al., 1998). Initial image processing was performed using custom-written software in MATLAB (Caltracer 3 Beta, available at our laboratory website). Regions of interest (ROIs) were drawn around each cell using a semiautomated algorithm based on fluorescence intensity (mean projection), florescence change (standard-deviation projection), and cell size and shape and were adjusted by visual inspection. Glial cells were excluded from further analysis using SR101 staining. Pixels were averaged within each ROI for each image frame. Baseline Ca^{2+} fluorescence was computed for each trial as the mean over 2 s prestimulus. Then, fluorescence values were converted to percentage change above baseline according to the following: $\Delta F/F = (F_1 - F)/F$ where F is the baseline fluorescence and F_1 is the instantaneous fluorescence signal averaged over 2 frames (~500 ms) after stimulus onset (F_{0+2}, F_{0+3}, where F_0 is stimulus onset frame; see Fig. 1*D*).

Neuropil (NP) subtraction was performed on all cell ROIs to correct for NP activity that could contaminate cellular measurements. NP subtraction was performed first by selecting a spherical neuropil mask surrounding each neuron (excluding adjacent masks; Jackson et al., 2016). Then we calculated separately $\Delta F/F$ for each cell ($\Delta F/F_{cell}$) and for its neuropil component ($\Delta F/F_{NP}$) and subtracted the neuropil component according to the following:

$$\Delta F/F = \Delta F/F_{cell} - \Delta F/F_{NP} \times 0.5$$

Responsiveness and reliability criteria were defined as described previously (Marshel et al., 2011). Briefly, neurons were considered responsive if their mean $\Delta F/F$ to any stimulus exceeded 6% and if they were found to be driven significantly by at least one visual stimulus against blank condition (*t* test with Bonferroni multiple-comparisons correction, $p < (0.05/n)$, where $n = 48$).

Reliability (δ) was determined according to the following:

$$\delta = \frac{\mu_{max} - \mu_{blank}}{\sigma_{max} - \sigma_{blank}}$$

where μ_{max} and σ_{max} are the mean and SDs of the response to the preferred stimulus, respectively, and μ_{blank} and σ_{blank} are the mean and SDs of the response to the blank stimulus, respectively. Neurons were considered reliable if $\delta > 1$. Only cells that demonstrated visual responsiveness and reliability were chosen for further analysis (typically 80–180 cells per FOV).

Horizontal bias was estimated as the difference between the fraction of neurons preferring horizontal orientations and the fraction of neurons preferring vertical orientations (Kreile et al., 2011).

Photostimulation artifact removal. During experiments with C1V1-expressing mice, we illuminated the FOV using a 590 nm LED pulses (420 ms at 33 Hz). Illumination time lasted less than the duration of two frames (see Fig. 2*F*) and these frames were not taken into account when computing the evoked responses of the cells (see Fig. 1*D*).

During experiments with ArchT-expressing mice, we used a 617 nm LED to illuminate the exposed cortex continuously for 1.4 s. The spread of light was not homogenous across the FOV; therefore, to remove the DC component of the LED illumination properly, we first calculated the changes in light detection between frames with LED-on and LED-off during recordings of spontaneous activity for 5–10 trials. Subtracting the acquired frames during LED-off from the following frames during LED-on and then averaging these frames resulted in a delta image that accounts for the DC shift that occurred due to the LED illumination. Then, we subtracted the delta image from every LED-on frame after acquisition, which resulted in Ca^{2+} signals clean of light contamination (see Fig. 6*F*).

Visual tuning. To calculate tuning curves, we averaged the evoked responses ($\Delta F/F$) over two frames after stimulus presentation (see Fig. 1*D*). Then, we averaged the response over the number of repetitions (5–10) per stimulus direction (12 directions). Direction tuning curves generated from OGB-1 fluorescence are comparable to those recorded with electrophysiological techniques (Kerlin et al., 2010; Marshel et al., 2011).

The orientation selectivity index (OSI) was computed as follows:

$$OSI = \frac{\mu_{max} - \mu_{orth}}{\mu_{max} + \mu_{orth}}$$

where μ_{max} is the mean response to the preferred direction (Pref) and μ_{orth} is the mean response to the orthogonal direction (Orth; average of both directions). Only cells that demonstrated OSI ≥ 0.3 were chosen for tuning analysis. The direction tuning curve was fitted with the sum of two Gaussians of identical width, constrained to peak 180° apart from one another, as follows:

$$R(\theta) = \alpha_0 + \alpha_1 e^{\frac{-(\theta-\theta_0)^2}{2\sigma^2}} + \alpha_2 e^{\frac{-(\theta-\theta_0+180)^2}{2\sigma^2}}$$

where $R(\theta)$ is the averaged response to gratings with direction θ, α_0 is computed as the mean $\Delta F/F$ of the four lowest points in the curve, α_1 and α_2 are the amplitudes of the two Gaussians, θ_0 is the preferred direction, and σ is the SD of the Gaussian function. Peak responses were the maximum $\Delta F/F$ values of the Gaussian-fit curve. Half-width at half-height was computed as follows:

$$HWHH = \sqrt{2ln2}\,\sigma$$

where σ is the SD of the Gaussian function.

SF tuning curves were calculated by fitting responses at the preferred direction of each cell to a difference-of-Gaussians (DOG) (Hawken and Parker, 1987; Kerlin et al., 2010). To compare the peak of the SF tuning curves based on the DOG fitting, we estimated upper and lower confidence intervals for the preferred SF by performing 500 Monte Carlo simulations (random sampling of trials of each stimulus with replacement) and included only neurons with 95% confidence interval of <1.5 octaves (Andermann et al., 2011). This criterion excluded an additional 31.2 ± 7.6% of the cells used for this analysis.

Immunohistochemistry

Immediately after *in vivo* experiments were completed, mice were overdosed with isoflurane and brains were quickly extracted into 4% PFA. Brains were fixed for 24 h, submerged in 30% sucrose for 2 d, and 25-μm-thick coronal sections were cut on a freezing microtome. Sections were blocked and permeabilized in PBS with 0.3% Triton X-100 and 1% bovine serum albumin (BSA) for 1 h, incubated with rabbit anti-GFP (1:500; Life Technologies) overnight, washed, incubated with Cy2-conjugated donkey anti-goat antibody (1:500; Jackson ImmunoResearch Laboratories) for 3.5 h, washed, and mounted. Antibodies were applied in PBS with 0.3% Triton X-100 and 1% BSA. Confocal micrographs were merged in ImageJ software and quantified to confirm the colocalization of tdTomato and VIP and then colocalization of opsins and tdTomato. Across three VIP-cre::TOM brains, 86.4% of detected tdTomato cells were immunoreactive (ir) for VIP and 94.9% of VIP-ir cells contained detectable tdTomato fluorescence (total 4445 coexpressing cells, 197 with VIP-ir only and 605 with tdTomato only). In three DIO-C1V1-YFP-injected brains, 97.4% (1029/1056) of YFP-containing cells coexpressed tdTomato. In four Flex-ArchT-GFP injected brains, 99.6% (822/825) of GFP-containing cells coexpressed tdTomato.

Slice electrophysiology and photostimulation in vitro

Coronal brain slices from P60–P100 VIP-cre animals expressing opsins were prepared and whole-cell patch-clamp recordings were performed according to standard methods (Karnani et al., 2016b). Briefly, 300-μm-thick acute brain slices were maintained in continuously gassed (95% O_2 and 5% CO_2) artificial CSF containing the following (in mM): 126 NaCl, 3 KCl, 2 $MgCl_2$, 2 $CaCl_2$, 1.1 NaH_2PO_4, 26 $NaHCO_3$, 0.1 pyruvic acid, 0.5 L-glutamine, 0.4 ascorbic acid, and 25 D-glucose. Patch pipettes (4–8 MΩ) were filled with K-gluconate-based intracellular solution and recordings were performed at room temperature. Photostimulation protocols *in vitro* were replicated from our *in vivo* experiments with the exact same LED-optic fiber system (see above), illuminating the slice at a distance of ~1 mm from the recording site.

Results

To investigate *in vivo* the local effect of VIP$^+$ interneurons on the cortical network in mouse V1, we used VIP-Cre mice with the tdTomato reporter mouse line (Ai14), yielding mice expressing tdTomato exclusively in VIP$^+$ cells. Because the majority of non-VIP$^+$ cells in layer 2/3 are pyramidal cells (Gonchar and Burkhalter, 1997), we will refer to non-VIP$^+$ cells as putative pyramidal cells. To manipulate the activity of VIP$^+$ cells, we used Cre-dependent rAAV viral injections into V1 of VIP-Cre mice (see Materials and Methods) and expressed either the light-activated cation channel C1V1 (Yizhar et al., 2011) to activate VIP$^+$ cells or the light-sensitive proton pump ArchT (Han et al., 2011) to suppress them.

VIP$^+$ cells show locked responses to visual stimuli

In lightly anesthetized or awake mice, we identified VIP$^+$ cells in layer 2/3 of visual cortex and, using two-photon Ca^{2+} imaging, monitored the activity of neuronal population (Stosiek et al., 2003; Ohki et al., 2005; Marshel et al., 2011; Miller et al., 2014) evoked by a brief visual stimulus presented in the contralateral visual field. We characterized the response dynamics of VIP$^+$ cells for each FOV by measuring the two-photon signal under 1040 nm excitation to detect the tdTomato-labeled VIP$^+$ cells (Fig. 1*A*), followed by optically recording Ca^{2+} signals of OGB-1 from the same FOV (Fig. 1*B*). We focused our optical recordings on neurons in upper layer 2/3 (~130–200 μm depth) because VIP$^+$ cells are highly prevalent at this depth (Prönneke et al., 2015). Consistent with earlier studies in mouse visual cortex (Kerlin et al., 2010; Mesik et al., 2015; Jackson et al., 2016), VIP$^+$ cells showed stimulus-locked responses (Fig. 1*C*). The averaged visual-evoked Ca^{2+} modulation of VIP$^+$ cells was lower than that of pyramidal cells, but significantly higher than baseline ($\Delta F/F$: 6.06 ± 1.54%, $n = 72$ VIP$^+$ cells in 9 mice; $p < 0.001$, t test).

Next, we analyzed the visual-evoked responses of each neuron in our FOV. Stimuli were square-wave drifting gratings presented for 420 ms and varied across 12 directions and four SFs. Short stimulus presentation preserved the response reliability of the cells ($\delta > 1$; see Materials and Methods) while keeping the Ca^{2+} responses below the saturation level (Fig. 1*D*). This allowed us to detect both increases and decreases in responses after circuit manipulations and enabled coupling two-photon imaging with photostimulation while keeping the signal free from light artifacts (see below, Fig. 2*F*, and Materials and Methods).

Based on the evoked responses, we calculated the SF- and direction tuning curve of each neuron in our FOV by averaging the response to each stimulus (Fig. 1*E*,*F*). Initial characterization of the local network showed an overrepresentation of the cells' preference for horizontal orientations (28.6 ± 7.1%, mean ± SEM, $n = 5$ mice; Fig. 1*G*, see Materials and Methods) in accordance with previous studies that found "horizontal bias" in mouse V1 largely in upper layer 2/3 (Kreile et al., 2011; Wertz et al., 2015). Second, we found that the SF response was mainly in the range of 0.02–0.04 cpd (Fig. 1*H*) with a median of 0.034 ± 0.004 cpd ($n = 5$ mice; mean ± SEM), similar to what was found in previous studies (Niell and Stryker, 2008; Gao et al., 2010; Kerlin et al., 2010; Marshel et al., 2011). VIP$^+$ cells followed the overall network tuning characteristics (Fig. 1*G*,*H*, bottom), although with weaker and less specific responses, as expected (Kerlin et al., 2010).

Optogenetic activation of VIP$^+$ cells alters network SF selectivity

We further investigated how VIP$^+$ cells affect the network activity during stimulus-evoked responses. To do so, we first activated VIP$^+$ cells by expressing C1V1 exclusively in VIP$^+$ cells (Fig. 2*A*,*B*). We used a photostimulation pulse train that produced high-fidelity firing in VIP$^+$ cells *in vitro* (590 nm, 150 ms, 33 Hz;

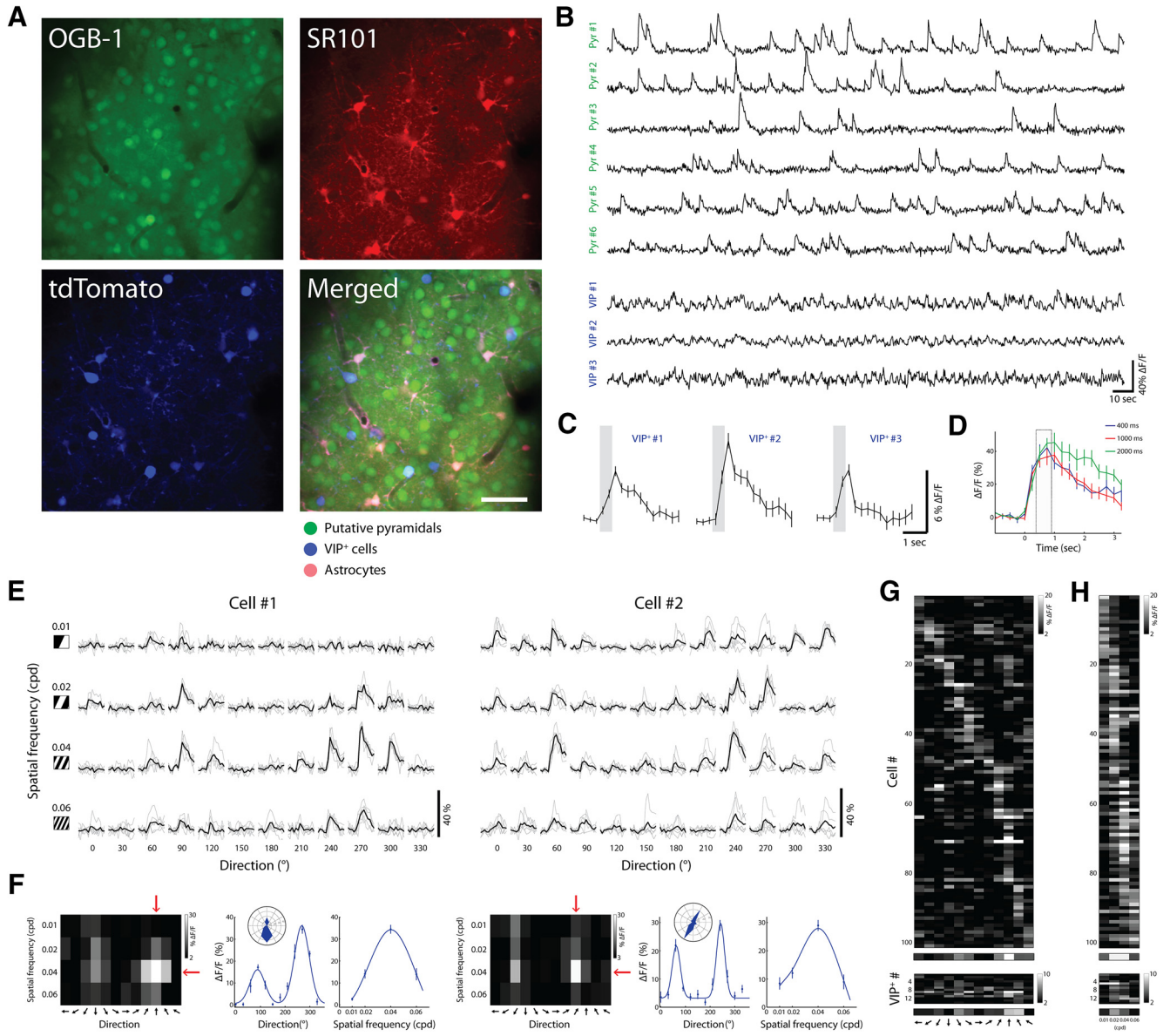

Figure 1. *In vivo* imaging of visual-evoked responses of layer 2/3 neurons. ***A***, Top, Two-photon image from a VIP-Cre x tdTomato mouse loaded with OGB-1 (left) and SR101 (right) in layer 2/3 of V1. Scale bar, 50 μm. Bottom, Same FOV at 1040 nm excitation showing VIP$^+$ cells expressing tdTomato (left) and the merged image of the three (right). ***B***, Ca^{2+} responses of putative pyramidal cells and VIP$^+$ cells during visual evoked activity using drifting gratings stimuli. ***C***, Averaged visually evoked Ca^{2+} responses of three VIP$^+$ cells (420 ms stimulus, averaged over 12 directions; shaded gray box). ***D***, Example of Ca^{2+} responses time course of one cell, evoked by its preferred stimulus at different stimulus durations (400, 1000, and 2000 ms). Tuning matrices (shown below) were generated by averaging $\Delta F/F$ over two frames after stimulus onset (F_{0+2}, F_{0+3}, where F_0 is stimulus onset frame) marked by gray box. ***E***, Ca^{2+} responses of two neurons displayed as a matrix of all stimulus conditions. Columns indicate the direction of motion of the gratings and rows indicate their SF. Each trial is shown in gray ($n = 5$); average response across trials of a given stimulus is shown in black. ***F***, Tuning matrix and tuning curves of the cells shown in ***E***. Left, Response matrices evoked by each stimulus shown in ***E***. Pixel intensity corresponds to the average $\Delta F/F$ over two frames after stimulus presentation and over five repetitions. Red arrows point to the preferred direction and preferred SF. Middle, Direction tuning curves illustrated in Cartesian and polar axes fitted with a double Gaussian. Right, SF tuning curves fitted with DOG (solid curve). Plots are mean ± SEM. ***G***, Top, Direction tuning of an example network showing a raster plot of putative pyramidal cells with OSI >0.3. Each pixel represents the mean response of a cell to 12 directions at its preferred SF. Cells are sorted according to the direction that drives the largest response. Bottom, Same for VIP$^+$ cells. ***H***, Top, SF tuning of the same network as in ***G***. Each pixel represents the mean response of a cell to 4 SFs of gratings moving in the preferred direction. Cells are sorted according to the SF driving the largest response. The averaged tuning curve of the network is shown below ($n = 101$ cells). Bottom, Same for VIP$^+$ cells and their average ($n = 14$ cells).

Fig. 2*C*) and observed *in vivo* network firing induced by photostimulation (Fig. 2*D*), presumably due to the disinhibitory effect of VIP$^+$ cells on the local circuit (Pi et al., 2013). Then, we presented various visual stimuli (full-field drifting gratings; ~114° × 140°; 420 ms) and on every other trial coupled visual stimulation with photostimulation (590 nm, 420 ms, 33 Hz; Fig. 2*E*). Visual stimuli were presented in a pseudorandom order (block randomized) to control for slow network fluctuations in sensitivity. Visual stimulation and the LED pulse train lasted <2 imaging frames, enabling subsequent detection of Ca^{2+} responses without light contamination (Fig. 2*F*). Comparison between control trials (visual stimulation only) and LED-on trials (visual + LED stimulation) revealed a significant alteration of the preferred responses of the cells (Fig. 2*G*). Upon activation of VIP$^+$ cells, responses driven by low SF (0.02 cpd) were decreased significantly ($p < 10^{-4}$, Wilcoxon signed-rank test; Fig. 2*H*, top), whereas responses driven by high SF (0.06 cpd) were increased significantly ($p < 0.005$, Wilcoxon signed-rank test; Fig. 2*H*, bot-

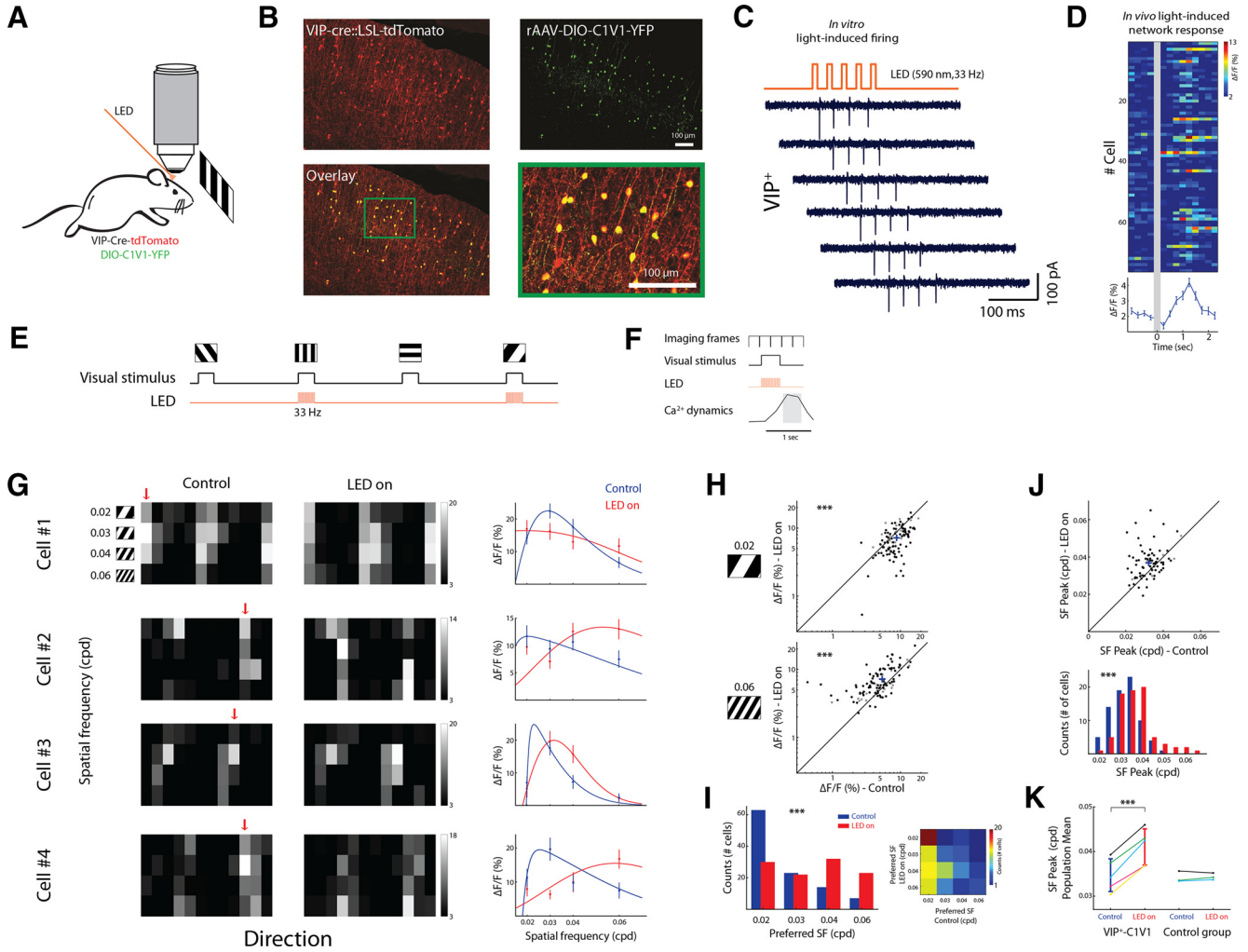

Figure 2. Optogenetic activation of VIP $^+$ cells alters SF tuning. ***A***, Schematic of *in vivo* imaging combined with wide-field photostimulation during presentation of drifting gratings. ***B***, Coronal section of a VIP-Cre x tdTomato mouse injected with DIO-C1V1-YFP. Top, Native expression of tdTomato shown in red; C1V1-YFP-expressing cells (anti-GFP immunostaining) are shown in green. Bottom, Overlaid image (green + red) and a zoomed area of the green rectangle shown on the overlaid image. ***C***, Example of cell-attached patch recordings in slice from the above mouse. Illumination settings were identical to *in vivo* experiments: 590 nm LED pulses at 33 Hz. ***D***, Top, *in vivo* light-induced responses ($n = 76$ cells, 8 trials). Photostimulation lasted 150 ms. Bottom, Averaged light-induced response across cells. ***E***, Experimental sequence: on interleaved trials visual stimuli were presented with photostimulation (LED-on) or without (control). Visual stimuli and LED pulses were synced and lasted 420 ms at 33 Hz; the interval between stimuli was 5 s. ***F***, Schematic of the frame acquisition and stimulation timings relative to the evoked Ca $^{2+}$ dynamics. ***G***, Tuning matrix and SF tuning curves of four cells. Pixel intensity corresponds to $\Delta F/F$ averaged over two frames after stimulus presentation and over eight repetitions. Left and middle, Evoked-response matrices under control and LED-on conditions, respectively. Red arrows point to the preferred direction. Right, SF tuning curves fitted with DOG. ***H***, Scatter plots from an example network ($n = 107$ cells) showing responses to gratings with 0.02 cpd (top) and 0.06 cpd (bottom) during control and LED-on conditions. Each circle represents a cell; cross represents population mean. Black circles depict cells with a significant change in their response amplitude to any stimulus ($n = 84$; t test with Bonferroni multiple-comparisons correction) and gray circles depict cells with no significant change ($n = 23$). ***I***, Left, Histograms of the cells' preferred SF in control (blue) and LED-on (red) conditions. Right, Confusion matrix showing an increase in the preferred SF of cells upon VIP $^+$ activation. ***J***, Top, Scatter plot of the response peak based on SF tuning curves fitted with DOG in control and LED-on conditions ($n = 76$ cells; only cells with 95% confidence interval <1.5 octaves were included in this analysis, see Materials and Methods). Bottom, Histogram of the SF response peak pooled into 10 bins, each 0.005 cpd wide, in control (blue) and LED-on (red) conditions. ***K***, Left, Population mean of the SF response peak estimated by DOG. Data are from five animals: three anesthetized (yellow, magenta, and cyan) and two awake (black and green). Right, Same for control mice ($n = 3$).

tom). Testing the distribution of preferred SFs (defined as the SF that evoked the maximum response) showed a significant shift toward higher frequencies during VIP $^+$ cell activation ($p < 10^{-4}$, Wilcoxon signed-rank test; Fig. 2*I*). A cell-by-cell multiple-comparisons between LED-on and control trials across all stimuli showed a significant alteration of response amplitude in 72.9 ± 7.3% of the cells ($p < 0.001$, t test with Bonferroni multiple-comparisons correction; $n = 5$ mice).

To obtain a finer estimation of the shift in preferred SF, we calculated the preferred SFs by fitting the data of each cell with DOG (Fig. 2*G*, right). This analysis also revealed a significant population shift of visual responses toward higher SFs upon VIP $^+$ cell activation ($p < 0.001$, Wilcoxon signed-rank test; only cells with 95% confidence interval < 1.5 octaves were analyzed here; see Materials and Methods; Fig. 2*J*). We supplemented our data from anesthetized animals ($n = 3$ mice) by repeating the experiment on awake animals ($n = 2$ mice) and found consistent results. There was no significant difference in any of the studied parameters between anesthetized and stationary awake animals (see Materials and Methods).

Overall, VIP $^+$ cell activation resulted in a significant positive shift in the mean preferred SF of 0.006 ± 0.001 cpd across the network population ($n = 5$ mice; $p < 0.05$, paired t test; Fig. 2*K*). To ensure that changes in SF tuning were caused by the optical

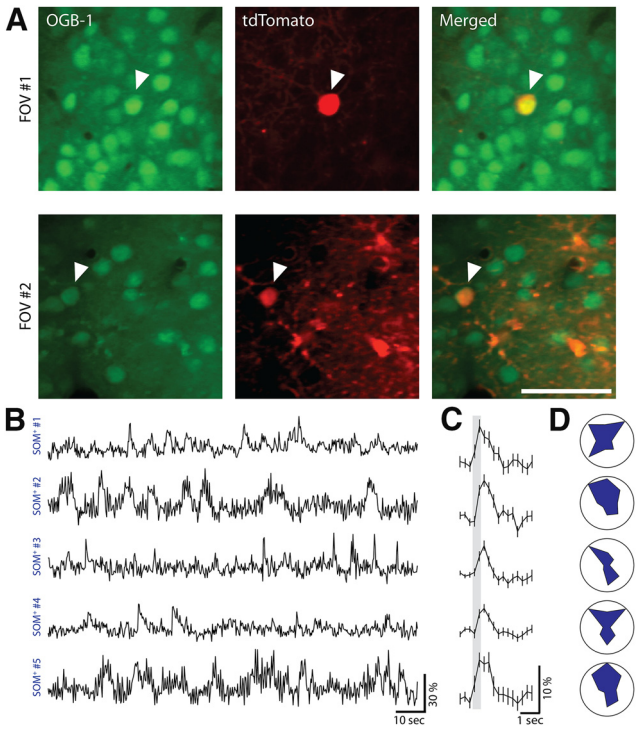

Figure 3. SOM$^+$ interneurons are active under light anesthesia. ***A***, Left, Two-photon images of two FOVs from SOM-cre::LSL-tdTomato mice bolus loaded with Oregon Green Bapta-1 AM (OGB-1) in upper layer 2/3 of V1 at 950 nm excitation. Middle, Same FOVs at 1040 nm excitation showing SOM$^+$ cells expressing tdTomato. Right, Merged images of the two. Scale bar, 50 μm. ***B***, Ca^{2+} responses of five SOM$^+$ cells from two mice measured under light isoflurane anesthesia showing active SOM$^+$ cells. ***C***, Averaged visual-evoked responses of five SOM$^+$ cells shown in ***A*** (420 ms stimulus marked with a shaded gray box, averaged over eight directions, eight trials each; mean ± SEM). ***D***, Polar plots of the normalized tuning curves for five SOM$^+$ cells shown in ***A*** and ***B*** (each point represents the mean response over eight trials normalized by the maximum response).

activation of VIP$^+$ cells rather than by light scatter or any other light-induced artifacts, we performed control experiments on animals that did not undergo viral delivery and found no significant change (Fig. 2*K*, $p > 0.05$; $n = 3$). Finally, one of the major targets of VIP$^+$ cells are SOM$^+$ cells. SOM$^+$ cell firing was found to be modulated significantly by urethane/chlorprothixene anesthesia (Adesnik et al., 2012) and consequently alter size tuning of V1 neurons under these conditions. Therefore, we verified that, under our experimental conditions (light isoflurane anesthesia and presentation of full-field visual stimuli), SOM$^+$ cells are indeed active (Fig. 3*A*,*B*) and demonstrate visual-evoked responses (9 SOM$^+$ cells in 3 mice; $p < 0.001$ for each cell; *t* test with Bonferroni multiple-comparisons corrections for any stimulus condition against blank; Fig. 3*C*) with direction tuning properties similar to previous studies (Fig. 3*D*) (Kerlin et al., 2010; Ma et al., 2010; Cottam et al., 2013).

Dependence of orientation tuning on SF

Next, we wanted to determine how manipulating VIP$^+$ cell activity affects the orientation tuning of putative pyramidal cells. We found that, in mouse visual cortex, orientation tuning of pyramidal cells depended on SF. We characterized the dependence and then studied the changes in network responses along the orientation/direction dimension during VIP$^+$ manipulation.

A fast and efficient way to study orientation tuning is to measure one-dimensional tuning curves and then estimate parameters derived from these curves [such as OSI or half-width at half-height (HWHH); see Materials and Methods]. In our experiments, we presented gratings with 12 directions, four SFs, and one TF (following a broader and more exhaustive search of parameters; data not shown). For each cell, we compared the direction tuning curve at its preferred SF with the tuning curve at non-optimum SFs; that is, either below or above the preferred SF (Fig. 4*A*).

Direction tuning curves at SF below the preferred SF had by definition reduced responses to the preferred direction, but they also showed increased responses to the orthogonal-to-preferred direction ($p < 10^{-5}$, Wilcoxon signed-rank test), a decrease in OSI values ($p < 10^{-7}$, Wilcoxon signed-rank test), and an increase in HWHH ($p < 10^{-3}$, Wilcoxon signed-rank test) (Fig. 4*B*). In addition, we observed a significant shift in the preferred orientation (because we sampled 12 directions between 0° to 360°, for this analysis, we subtracted 180° from the preferred direction of cells that had preferred direction >180°) of 32.0 ± 4.2° (mean ± SEM, $n = 5$ mice; $p < 0.02$, Wilcoxon signed-rank test). Direction tuning curves measured with SF above the preferred SF had a decreased response to the preferred direction, no change in orthogonal-to-preferred responses ($p > 0.05$), a significant decrease in OSI values ($p < 10^{-3}$, Wilcoxon signed-rank test), and no change in HWHH or in the preferred direction ($p > 0.05$, Wilcoxon signed-rank test). Dependence between orientation tuning and SF has been suggested previously in primates and cats (Andrews and Pollen, 1979; Vidyasagar and Sigüenza, 1985; Webster and De Valois, 1985; Zhu et al., 2010).

Optogenetic activation of VIP$^+$ cells alters orientation tuning of pyramidal cells

Given the observed dependence of orientation tuning on SF, we sought to study the orientation tuning of pyramidal cells during activation of VIP$^+$ cells. We compared direction tuning curves of each cell at its preferred SF during control and during VIP$^+$-activated (LED-on) conditions (Fig. 5*A*,*B*). We examined four parameters of the tuning curves: (1) the response amplitude to the preferred direction (the maximum of the 2D Gaussian curve); (2) the response amplitude to the orthogonal-to-preferred direction (the mean $\Delta F/F$ of ±90° from the preferred direction); (3) OSI; and (4) HWHH (Fig. 5*C*). During VIP$^+$ activation (LED-on), responses to the preferred direction decreased ($p < 10^{-7}$, Wilcoxon signed-rank test, $n = 5$ mice), whereas responses to the orthogonal increased ($p < 0.005$, Wilcoxon signed-rank test); OSI values decreased ($p < 10^{-3}$, Wilcoxon signed-rank test), and HWHH increased ($p < 10^{-4}$, Wilcoxon signed-rank test).

The observed changes in the direction tuning curves of pyramidal cells upon activation of VIP$^+$ cells resembled changes that occurred with a lower-than-optimal stimulus SF. Such changes are consistent with our finding that VIP$^+$ cells control the SF selectivity of the network. As shown in Figure 4, when the stimulus was below the preferred SF, orientation tuning curves exhibited a specific alteration in parameters. These included a decrease in the preferred response, an increase in the orthogonal response, a decrease in OSI, and an increase in HWHH. These same changes also occurred when we activated VIP$^+$ cells and examined responses to the optimal stimulus (defined by the control condition). This result implies that, upon activation of VIP$^+$ cells, the presented stimulus was no longer optimal due to changes in the SF sensitivity of the cells and of the network. Rather, the pattern of responses resembled those evoked by stimuli with SF below the optimal, consistent with our findings that the SF tuning of layer 2/3 pyramidal cells changed toward higher frequencies during VIP$^+$ activation.

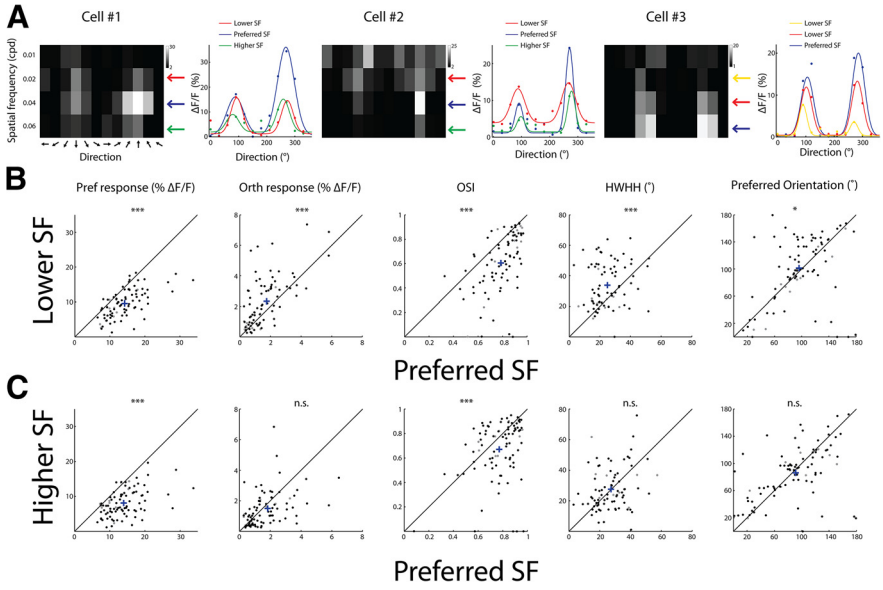

Figure 4. Dependencies between orientation tuning and SF. ***A***, Examples of three cells' tuning matrices and direction tuning curves at different SFs. Left, Matrices of the response evoked by each stimulus. Pixel intensity corresponds to the average $\Delta F/F$ over two frames after stimulus presentation and over five repetitions. Arrows on the right point to different SFs color coded according to the curves on the right. Right, Direction tuning curves fitted with a double Gaussian. ***B***, Comparison of tuning parameters between the preferred SF of each cell and one lower SF. Shown are scatter plots of cells that had preferred SF $\geq$0.02 cpd ($n = 83$ cells). Each circle represents a cell and cross represents population average. Shown from left to right are the response amplitude ($\Delta F/F$) to the preferred direction (Pref), the response amplitude to the orthogonal direction (Orth), OSI, HWHH, and the preferred orientation (for this analysis, we subtracted 180° from the preferred direction of cells that had preferred direction >180°). ***C***, Comparison of tuning parameters between the preferred SF of each cell and one higher SF. Scatter plots of cells that had preferred SF of $\leq$0.04 cpd ($n = 88$ cells). Shown are the same parameters as in ***B***. Black circles depict cells with a significant change in their response amplitude to any stimulus between the preferred SF and nonpreferred SF and gray circles depict cells with no significant change ($p < 0.001$, *t* test with Bonferroni multiple-comparisons correction).

Finally, these changes in the tuning curves cannot be explained by a simple response normalization (either subtractive or divisive) in which the responses to the preferred direction and the orthogonal-to-preferred direction increase together or decrease together. What was observed here was a decrease in the preferred direction along with an increase in the orthogonal direction.

Optogenetic suppression of VIP$^+$ cells alters network SF selectivity

We also studied the effect of suppressing VIP$^+$ cells on visual responses of layer 2/3 pyramidal cells. To suppress VIP$^+$ cells, we used the optical silencer ArchT (Han et al., 2011) expressed exclusively in VIP$^+$ cells using viral delivery (Fig. 6*A*). In slice recordings from VIP$^+$ cells expressing ArchT, we observed a hyperpolarization of 14.6 ± 9.3 mV ($n = 12$, mean ± SD) during a continuous LED pulse (1 s), followed by a rebound firing that occurred 73 ± 12 ms after the LED was turned off ($n = 13$; Fig. 6*B*). *In vivo*, we could confirm rebound spiking of VIP$^+$ cells by a significant modulation in Ca^{2+} signal of some cells immediately after a light pulse (2 s, Fig. 6*C*; 1.4 s, Fig. 6*D*), presumably due to the disinhibitory effect of VIP$^+$ cells on the local circuit. To avoid the rebound spikes, we presented a short visual stimulation (670 ms) accompanied at each alternate trial with a longer wide-field photostimulation (617 nm LED; 1.4 s) such that we could measure the evoked responses during the time that the LED was still on (see Materials and Methods for photostimulation artifact removal; Fig. 6*E*,*F*).

Multiple comparisons between control (visual stimulation only) and LED-on trials (visual + LED stimulation) across all stimuli showed a significant change in response amplitude in 63.5 ± 6.9% of the cells (*t* test with Bonferroni multiple-comparisons correction; $p < 0.001$; $n = 5$ mice; Fig. 6*G*,*H*). The distribution of preferred SF showed a significant shift toward lower frequencies during VIP$^+$ cell suppression ($p < 0.01$, Wilcoxon signed-rank test; Fig. 6*H*) and tuning curves fitted with DOG also showed a significant reduction in the peak frequency of putative pyramidal cells ($p < 0.005$, Wilcoxon signed-rank test; Fig. 6*I*). For all animals, upon suppression of VIP$^+$ cells, we observed a significant negative shift in the mean preferred SF across the network population of 0.004 ± 0.001 cpd ($p < 0.05$, paired *t* test; $n = 5$ mice, 4 anesthetized, 1 awake; Fig. 6*J*). Similar to our observations when VIP$^+$ cells were activated, we also analyzed orientation tuning curves of each cell at its preferred SF and identified a significant altering of the tuning parameters (Fig. 6*K*). Specifically, the preferred responses decreased ($p < 10^{-7}$), OSI decreased ($p < 10^{-6}$), and HWHH slightly increased ($p < 0.05$). Control animals that did not undergo viral delivery and were presented with drifting gratings with 1 SF (0.04 cpd) and 12 directions during the same photostimulation protocol did not show a significant change in any orientation tuning parameter ($n = 3$ mice, $p > 0.05$ for Pref, Orth, OSI, and HWHH). Collectively, these results support the hypothesis that VIP$^+$ cells control the SF selectivity of the network.

Discussion

We used two-photon Ca^{2+} imaging in mouse V1 to test the role of VIP$^+$ interneurons in processing visual information. To do so, we measured tuning properties of cells in V1 while selectively activating or suppressing responses of VIP$^+$ cells. We demonstrate that this distinct class of interneurons has a specific role in processing sensory stimuli and exerts a fundamental effect on the SF tuning properties of pyramidal cells in upper layer 2/3. First, enhancing the activity of VIP$^+$ cells during responses to visual stimuli caused a significant change in the network SF selectivity. This was evident in the increased responses to high SFs, decreased responses to low SFs, and a shift in the peak of the SF curve toward higher SFs of ~70% of the tuned cells. Orientation tuning curves were also altered, as one would expect from the SF effect, resulting in a reduction in OSI values and broadening of the curves, mimicking tuning curves evoked by stimuli with nonoptimal SF. Upon suppression of VIP$^+$ cells, we found a shift toward lower SFs of ~60% of the tuned cells and, again, weakening of the orientation tuning seen as a decrease in OSI values. These findings align well with the recent demonstration that chronic elevation of VIP$^+$ cell activity enhanced visual acuity and increased the cortical evoked potential to stimuli of higher spatial frequencies (Mardinly et al., 2016).

In visual cortex, previous work has indicated that activation of VIP$^+$ cells for a long duration (4 s) produced no significant effect on tuning width or direction selectivity index of V1 cells (but

changes in OSI were not reported; Lee et al., 2012). These results are at odds with our findings and might result from differences in experimental conditions such as stimulus duration, different sampling of stimulus SF, or the use of a red shifted opsin here and longer wavelength light, which penetrates deeper into tissue. However, VIP$^+$ cell activation was found to mediate top-down modulation by intracortical feedback from frontal cortex that improves visual discrimination (Zhang et al., 2014). In particular, Zhang et al. (2014) showed a spatially specific modulation of visual responses, which is a hallmark of selective attention. The spatial profile of this modulation consisted of a center facilitation and a suppressive surround, resembling effects of top-down attention in primates (for review, see Desimone and Duncan, 1995; Chen et al., 2008; Sundberg et al., 2009). Attention involves modulation of visual cortex responses exerted by brain-wide signals outside the visual system per se. These forms of modulation may arise due to specific feedback from higher brain areas (e.g., the frontal cortex) or as a result of global state changes such as locomotion or pupil dilation. VIP$^+$ cells have a general role in mediating these high-excitability states in the cortex and, furthermore, blocking VIP$^+$ cell output using pharmacogenetics resulted in reduced spontaneous activity in the cortex under anesthesia, during awake immobility, and during locomotion (Jackson et al., 2016).

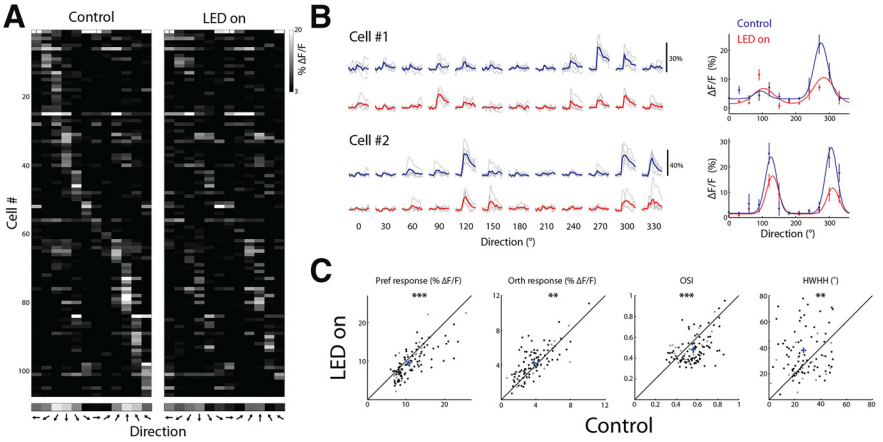

Figure 5. Optogenetic activation of VIP$^+$ cells alters orientation selectivity. ***A***, Direction tuning matrix of an example network from a VIP-cre::LSL-tdTomato mouse injected with DIO-C1V1-YFP showing a raster plot of putative pyramidal cells with OSI >0.3 ($n = 107$) in control and LED-on conditions. Each pixel represents the mean response ($\Delta F/F$) of a cell to 12 directions at its preferred SF. Cells are sorted according to the direction that drives the largest response in the control condition. Bottom, Averaged tuning curve of the network. ***B***, Left, Ca^{2+} traces of two examples of responsive neurons displayed as a matrix of all direction of motion at the preferred SF. Each trial is shown in gray ($n = 5$) and the average response across trials of a given stimulus is shown in blue or red in the control or LED-on condition, respectively. Right, Tuning curves fitted with a double Gaussian of the cells shown on the left. Plots are mean ± SEM. ***C***, Scatter plots comparing various parameters in control and LED-on conditions. Shown are the response amplitude ($\Delta F/F$) to the preferred direction (Pref), the response amplitude to the orthogonal direction (Orth), OSI, and HWHH. Each circle represents a cell and cross represents population average. Black circles depict cells with a significant change in their response amplitude to any stimulus between the control and LED-on condition ($n = 86$) and gray circles depict cells with no significant change ($n = 21$; $p < 0.001$; *t* test with Bonferroni multiple-comparisons correction).

Our findings here further show that VIP$^+$ cells not only modulate the network gain, but also have a fundamental effect on the network coding—they regulate the SF tuning of pyramidal neurons and thus the spatial resolution of the network. In fact, the effect of attention on spatial resolution has been well demonstrated in humans using different tasks such as visual search tasks, acuity tasks, or texture segmentation tasks (Yeshurun and Carrasco, 1998; for review, see Anton-Erxleben and Carrasco, 2013). Effects of attention are also accompanied by changes in the subjective experience of spatial features; for example, attention increases the perceived SF (Abrams et al., 2010). Physiological studies in primates also show that attention operates by changing the spatial integration of single neurons by contracting their RFs (Moran and Desimone, 1985). Because VIP$^+$ interneurons are affected directly by neuromodulators (Fu et al., 2014) that are released during attentional paradigms, our results now provide a clear circuit mechanism for these functional effects of attention on spatial resolution.

However, a study investigating tuning properties of V1 neurons in awake mice (Andermann et al., 2011) did not observe a significant change in SF preference with locomotion. One possible reason may be that, during periods when VIP$^+$ cells are highly active (e.g., locomotion), other classes of cholinosensitive cortical neurons are modulated, thus maintaining a balance between excitation and inhibition. In contrast, direct manipulation of VIP$^+$ neurons in isolation may violate the excitation/inhibition balance, therefore revealing a significant change in tuning. Moreover, another study showed that the SF tuning in mouse V1 changes substantially over time such that the preferred SF shifts from low to high at longer latencies (Vreysen et al., 2012). Because activation of VIP$^+$ cells suppresses short-latency and enhances long-latency responses (Pi et al., 2013), the elevation in SF preference that we observed after VIP$^+$ cell activation could be explained by the change in the neurons' SF sensitivity with response latency. To test this, electrophysiological recordings are needed to capture activity at higher temporal resolution and inspect changes in firing rate precisely over time.

VIP$^+$ cells function primarily through disinhibition of pyramidal cells (Lee et al., 2013; Pi et al., 2013), which largely results from inhibition of SOM$^+$ cells, which have dense inhibitory contacts on pyramidal cell dendrites (Pfeffer et al., 2013). However, the inhibitory influence of VIP$^+$ cells on pyramidal cells is possible, but has not been well characterized, and might result from either a direct inhibition of VIP$^+$ on pyramidal cells or a trisynaptic loop from VIP$^+$ to SOM$^+$, SOM$^+$ to PV$^+$, and PV$^+$ to pyramidal cells. The latter is supported by a recent study (Cottam et al., 2013) demonstrating how inhibition of SOM$^+$ onto PV$^+$ cells affects visual processing of pyramidal cells. That study found that, during visual stimulation, activation of SOM$^+$ cells suppressed PV$^+$ cell spiking at least twice as powerfully as pyramidal cell spiking. In addition, a recent study (Adesnik et al., 2012) demonstrated that SOM$^+$ cells contribute to surround suppression in the superficial layers of mouse visual cortex. Therefore, VIP$^+$ cells may play a role in controlling center-surround interactions by inhibiting SOM$^+$ cells and consequently increasing excitation to the center while disinhibiting PV$^+$ cells. The feasibility of this trisynaptic loop VIP$^+$ → SOM$^+$ → PV$^+$ is established by connectivity probabilities (Pfeffer et al., 2013), but its functional role has not yet been tested.

VIP$^+$ axons are narrower than SOM$^+$ or PV$^+$ axons, are vertically elongated, and tend to descend away from the pia (Kawaguchi and Kubota, 1996; Bayraktar et al., 2000; Tahvildari

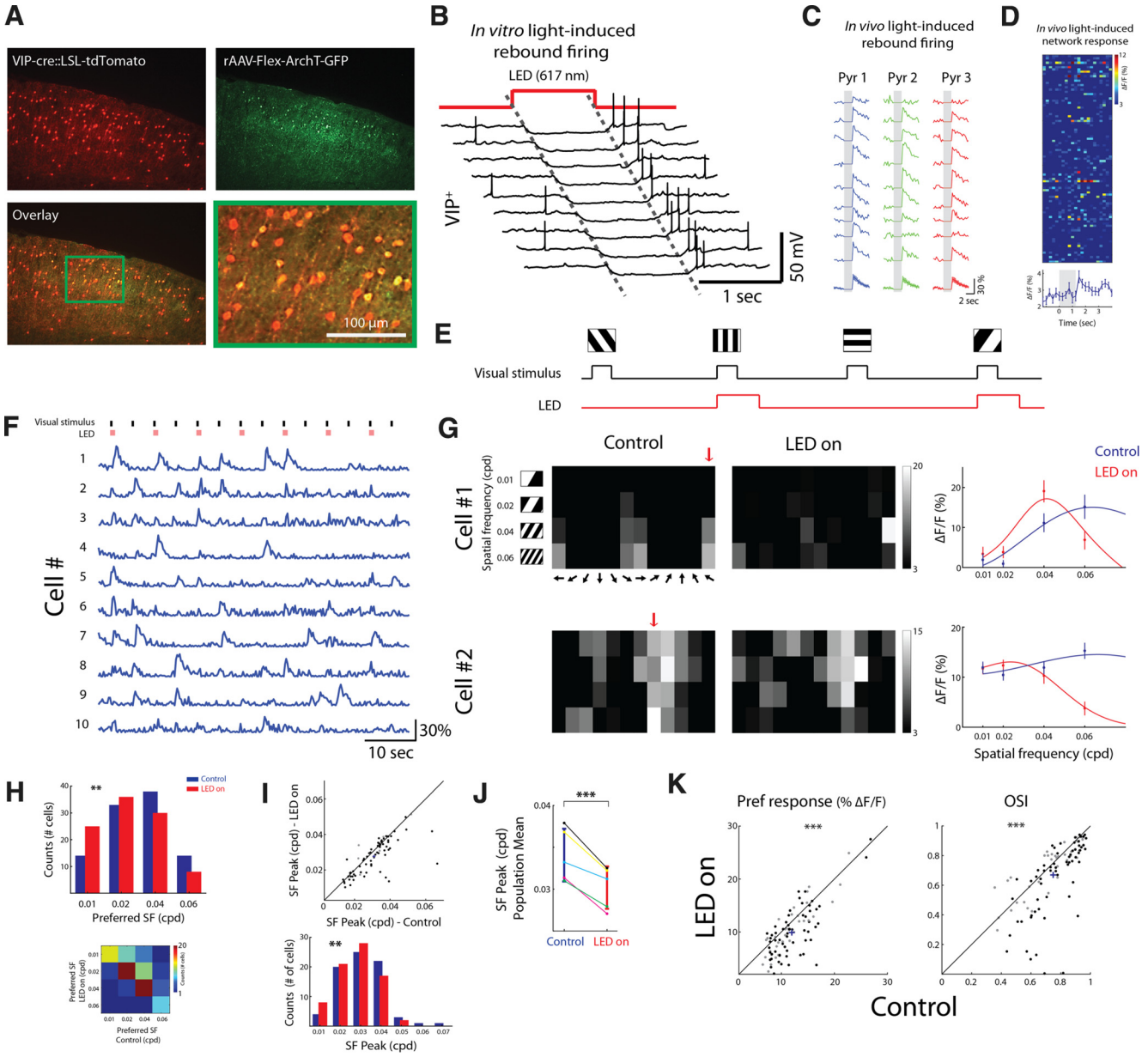

Figure 6. Optogenetic suppression of VIP $^{+}$ cells alters SF and orientation tuning. ***A***, Top, Coronal section of a VIP-Cre x tdTomato mouse injected with a FLEX-ArchT-GFP. The native expression of tdTomato is shown in red; ArchT-GFP-expressing cells (anti-GFP immunostaining) are shown in green. Bottom, Overlaid image (green + red) and a magnified area of the green rectangle. ***B***, Example of whole-cell patch-clamp recordings in slices from the above mice. Illumination settings were similar to *in vivo* experiments (see Materials and Methods). ***C***, Example of *in vivo* Ca^{2+} responses evoked after suppression of VIP $^{+}$ cells, presumably by the rebound firing of VIP $^{+}$ cells that occur after photostimulation. Gray shaded area denotes photostimulation frames (2 s; emission was collected in this example with a 535/50 nm filter, therefore frames during photostimulation were zeroed for presentation purposes due to light artifact). ***D***, Top, *In vivo* light-induced network response ($n = 93$ cells, 9 trials). Photostimulation lasted 1.4 s. Bottom, Averaged response across cells. ***E***, Imaging protocol. On interleaved trials, visual stimuli were presented either with photostimulation (red; LED-on) or without (control) in a pseudorandom order (block randomized). Visual stimuli lasted 670 ms; LED pulses were locked to visual stimuli and lasted 1.4 s; the interval between stimuli was 4 s. ***F***, Ca^{2+} responses of 10 putative pyramidal cells during visual stimulation and photostimulation. Top, Visual stimuli are shown in black (670 ms) and photostimuli in pink (1.4 s; for photostimulation artifact removal, see Materials and Methods). ***G***, Tuning matrix and SF tuning curves of two example cells. Left and middle, Matrices of the evoked responses to each stimulus under control and LED-on conditions, respectively. Red arrows point to the preferred direction. Right, SF tuning curves fitted with DOG. ***H***, Top, Histograms of the cells' preferred SF in control (blue) and LED-on (red) conditions ($n = 99$ cells). Bottom, Confusion matrix showing a decrease in the cells' preferred SF upon VIP $^{+}$ suppression. ***I***, Top, Scatter plots from an example network showing the response peak of the SF tuning curves fitted with DOG in control and LED-on conditions ($n = 76$ cells; only cells with 95% confidence interval <1.5 octaves were included in this analysis; see Materials and Methods). Each circle represents a cell; cross represents population average. Black circles depict cells with a significant change in their response amplitude to any stimulus and gray circles depict cells with no significant change ($p < 0.001$, *t* test with Bonferroni multiple-comparisons correction). Bottom, Histogram of the SF response peak pooled into 7 bins, each 0.01 cpd wide, in control (blue) and LED-on (red) conditions. ***J***, Population mean of the SF response peak estimated by DOG. Data are pooled from five animals: four anesthetized and one awake (black line). ***K***, Scatter plots comparing orientation tuning parameters in control and LED-on conditions. Shown are the response amplitude ($\Delta F/F$) to the preferred direction (Pref) and OSI.

et al., 2012; Karnani et al., 2016b). These axonal characteristics may restrict the area of effect of a single VIP $^{+}$ cell to a small cylindrical volume of cortex and, indeed, activation of a single VIP $^{+}$ cell is sufficient to affect a small local cortical region (~120 μm radius; Karnani et al., 2016b). This local effect might serve center-surround interactions and mediate selective attention modulations (Womelsdorf et al., 2006; Anton-Erxleben et al., 2009; Sundberg et al., 2009).

Results from this study add to existing evidence demonstrating that orientation and SF selectivity in the cortex are not solely a reflection of the excitatory projections from the LGN, as originally proposed by Hubel and Wiesel (1962). Rather, it is a property shaped by the entire visual system that is initiated in LGN (Piscopo et al., 2013), regulated locally within the cortex, and involves specific forms of intracortical GABAergic inhibition (for reviews, see Shapley et al., 2003; Alitto and Dan, 2010). Efficient feature selectivity is achieved by local mechanisms that allow for a dynamic modulation of cortical tuning and are engaged selectively during visual attention (Womelsdorf et al., 2006; Anton-Erxleben et al., 2009; Sundberg et al., 2009). Our data show that VIP^+ interneurons play a key role in regulating this complex modulation and highlight how neuronal circuits can shape incoming sensory information dynamically, crafting selective responses that are behaviorally important for the animal.

References

Abrams J, Barbot A, Carrasco M (2010) Voluntary attention increases perceived spatial frequency. Atten Percept Psychophys 72:1510–1521. CrossRef Medline

Adesnik H, Bruns W, Taniguchi H, Huang ZJ, Scanziani M (2012) A neural circuit for spatial summation in visual cortex. Nature 490:226–231. CrossRef Medline

Alitto HJ, Dan Y (2010) Function of inhibition in visual cortical processing. Curr Opin Neurobiol 20:340–346. CrossRef Medline

Andermann ML, Kerlin AM, Roumis DK, Glickfeld LL, Reid RC (2011) Functional specialization of mouse higher visual cortical areas. Neuron 72:1025–1039. CrossRef Medline

Andrews BW, Pollen DA (1979) Relationship between spatial frequency selectivity and receptive field profile of simple cells. J Physiol 287:163–176. CrossRef Medline

Anton-Erxleben K, Carrasco M (2013) Attentional enhancement of spatial resolution: linking behavioural and neurophysiological evidence. Nat Rev Neurosci 14:188–200. CrossRef Medline

Anton-Erxleben K, Stephan VM, Treue S (2009) Attention reshapes center-surround receptive field structure in macaque cortical area MT. Cereb Cortex 19:2466–2478. CrossRef Medline

Atallah BV, Bruns W, Carandini M, Scanziani M (2012) Parvalbumin-expressing interneurons linearly transform cortical responses to visual stimuli. Neuron 73:159–170. CrossRef Medline

Bayraktar T, Welker E, Freund TF, Zilles K, Staiger JF (2000) Neurons immunoreactive for vasoactive intestinal polypeptide in the rat primary somatosensory cortex: morphology and spatial relationship to barrel-related columns. J Comp Neurol 420:291–304. Medline

Brainard DH (1997) The Psychophysics Toolbox. Spat Vis 10:433–436. CrossRef Medline

Chen Y, Martinez-Conde S, Macknik SL, Bereshpolova Y, Swadlow HA, Alonso JM (2008) Task difficulty modulates the activity of specific neuronal populations in primary visual cortex. Nat Neurosci 11:974–982. CrossRef Medline

Cottam JC, Smith SL, Häusser M (2013) Target-specific effects of somatostatin-expressing interneurons on neocortical visual processing. J Neurosci 33:19567–19578. CrossRef Medline

Desimone R, Duncan J (1995) Neural mechanisms of selective visual attention. Annu Rev Neurosci 18:193–222. CrossRef Medline

Fu Y, Tucciarone JM, Espinosa JS, Sheng N, Darcy DP, Nicoll RA, Huang ZJ, Stryker MP (2014) A cortical circuit for gain control by behavioral state. Cell 156:1139–1152. CrossRef Medline

Gao E, DeAngelis GC, Burkhalter A (2010) Parallel input channels to mouse primary visual cortex. J Neurosci 30:5912–5926. CrossRef Medline

Gonchar Y, Burkhalter A (1997) Three distinct families of GABAergic neurons in rat visual cortex. Cereb Cortex 7:347–358. CrossRef Medline

Han X, Chow BY, Zhou H, Klapoetke NC, Chuong A, Rajimehr R, Yang A, Baratta MV, Winkle J, Desimone R, Boyden ES (2011) A high-light sensitivity optical neural silencer: development and application to optogenetic control of non-human primate cortex. Front Syst Neurosci 5:18. CrossRef Medline

Hawken MJ, Parker AJ (1987) Spatial properties of neurons in the monkey striate cortex. Proc R Soc Lond B Biol Sci 231:251–288. CrossRef Medline

Hubel DH, Wiesel TN (1962) Receptive fields, binocular interaction and functional architecture in the cat's visual cortex. J Physiol 160:106–154. CrossRef Medline

Jackson J, Ayzenshtat I, Karnani MM, Yuste R (2016) VIP+ interneurons control neocortical activity across brain states. J Neurophysiol 115:3008–3017. CrossRef Medline

Karnani MM, Jackson J, Ayzenshtat I, Tucciarone J, Manoocheri K, Snider WG, Yuste R (2016a) Cooperative subnetworks of molecularly similar interneurons in mouse neocortex. Neuron 90:86–100. CrossRef Medline

Karnani MM, Jackson J, Ayzenshtat I, Hamzehei Sichani A, Manoocheri K, Kim S, Yuste R (2016b) Opening holes in the blanket of inhibition: localized lateral disinhibition by VIP interneurons. J Neurosci 36:3471–3480. CrossRef Medline

Katzner S, Busse L, Carandini M (2011) GABAA inhibition controls response gain in visual cortex. J Neurosci 31:5931–5941. CrossRef Medline

Kawaguchi Y, Kubota Y (1996) Physiological and morphological identification of somatostatin- or vasoactive intestinal polypeptide-containing cells among GABAergic cell subtypes in rat frontal cortex. J Neurosci 16:2701–2715. Medline

Kerlin AM, Andermann ML, Berezovskii VK, Reid RC (2010) Broadly tuned response properties of diverse inhibitory neuron subtypes in mouse visual cortex. Neuron 67:858–871. CrossRef Medline

Kleiner M, Brainard D, Pelli D (2007) "What's new in Psychtoolbox-3?" Paper presented at the Thirtieth European Conference on Visual Perception, Arezzo, Italy.

Ko H, Hofer SB, Pichler B, Buchanan KA, Sjöström PJ, Mrsic-Flogel TD (2011) Functional specificity of local synaptic connections in neocortical networks. Nature 473:87–91. CrossRef Medline

Kreile AK, Bonhoeffer T, Hübener M (2011) Altered visual experience induces instructive changes of orientation preference in mouse visual cortex. J Neurosci 31:13911–13920. CrossRef Medline

Kyriazi HT, Carvell GE, Brumberg JC, Simons DJ (1996) Quantitative effects of GABA and bicuculline methiodide on receptive field properties of neurons in real and simulated whisker barrels. J Neurophysiol 75:547–560. Medline

Lee SH, Kwan AC, Zhang S, Phoumthipphavong V, Flannery JG, Masmanidis SC, Taniguchi H, Huang ZJ, Zhang F, Boyden ES, Deisseroth K, Dan Y (2012) Activation of specific interneurons improves V1 feature selectivity and visual perception. Nature 488:379–383. CrossRef Medline

Lee SH, Kwan AC, Dan Y (2014) Interneuron subtypes and orientation tuning. Nature 508:E1–E2. CrossRef Medline

Lee S, Kruglikov I, Huang ZJ, Fishell G, Rudy B (2013) A disinhibitory circuit mediates motor integration in the somatosensory cortex. Nat Neurosci 16:1662–1670. CrossRef Medline

Liu BH, Li P, Li YT, Sun YJ, Yanagawa Y, Obata K, Zhang LI, Tao HW (2009) Visual receptive field structure of cortical inhibitory neurons revealed by two-photon imaging guided recording. J Neurosci 29:10520–10532. CrossRef Medline

Ma WP, Liu BH, Li YT, Huang ZJ, Zhang LI, Tao HW (2010) Visual representations by cortical somatostatin inhibitory neurons–selective but with weak and delayed responses. J Neurosci 30:14371–14379. CrossRef Medline

Mardinly AR, Spiegel I, Patrizi A, Centofante E, Bazinet JE, Tzeng CP, Mandel-Brehm C, Harmin DA, Adesnik H, Fagiolini M, Greenberg ME (2016) Sensory experience regulates cortical inhibition by inducing IGF1 in VIP neurons. Nature 531:371–375. CrossRef Medline

Marshel JH, Garrett ME, Nauhaus I, Callaway EM (2011) Functional specialization of seven mouse visual cortical areas. Neuron 72:1040–1054. CrossRef Medline

Mesik L, Ma WP, Li LY, Ibrahim LA, Huang ZJ, Zhang LI, Tao HW (2015) Functional response properties of VIP-expressing inhibitory neurons in mouse visual and auditory cortex. Front Neural Circuits 9:22. CrossRef Medline

Miller JE, Ayzenshtat I, Carrillo-Reid L, Yuste R (2014) Visual stimuli recruit intrinsically generated cortical ensembles. Proc Natl Acad Sci U S A 111:E4053–4061. CrossRef Medline

Moran J, Desimone R (1985) Selective attention gates visual processing in the extrastriate cortex. Science 229:782–784. CrossRef Medline

Niell CM, Stryker MP (2008) Highly selective receptive fields in mouse visual cortex. J Neurosci 28:7520–7536. CrossRef Medline

Nimmerjahn A, Kirchhoff F, Kerr JN, Helmchen F (2004) Sulforhodamine

101 as a specific marker of astroglia in the neocortex in vivo. Nat Methods 1:31–37. CrossRef Medline

Ohki K, Chung S, Ch'ng YH, Kara P, Reid RC (2005) Functional imaging with cellular resolution reveals precise micro-architecture in visual cortex. Nature 433:597–603. CrossRef Medline

Pelli DG (1997) The VideoToolbox software for visual psychophysics: transforming numbers into movies. Spat Vis 10:437–442. CrossRef Medline

Pfeffer CK, Xue M, He M, Huang ZJ, Scanziani M (2013) Inhibition of inhibition in visual cortex: the logic of connections between molecularly distinct interneurons. Nat Neurosci 16:1068–1076. CrossRef Medline

Pi HJ, Hangya B, Kvitsiani D, Sanders JI, Huang ZJ, Kepecs A (2013) Cortical interneurons that specialize in disinhibitory control. Nature 503:521–524. CrossRef Medline

Piscopo DM, El-Danaf RN, Huberman AD, Niell CM (2013) Diverse visual features encoded in mouse lateral geniculate nucleus. J Neurosci 33:4642–4656. CrossRef Medline

Prönneke A, Scheuer B, Wagener RJ, Möck M, Witte M, Staiger JF (2015) Characterizing VIP neurons in the barrel cortex of VIPcre/tdTomato mice reveals layer-specific differences. Cereb Cortex 25:4854–4868. CrossRef Medline

Reimer J, Froudarakis E, Cadwell CR, Yatsenko D, Denfield GH, Tolias AS (2014) Pupil fluctuations track fast switching of cortical states during quiet wakefulness. Neuron 84:355–362. CrossRef Medline

Shapley R, Hawken M, Ringach DL (2003) Dynamics of orientation selectivity in the primary visual cortex and the importance of cortical inhibition. Neuron 38:689–699. CrossRef Medline

Sillito AM (1975) The effectiveness of bicuculline as an antagonist of GABA and visually evoked inhibition in the cat's striate cortex. J Physiol 250:287–304. CrossRef Medline

Sillito AM (1979) Inhibitory mechanisms influencing complex cell orientation selectivity and their modification at high resting discharge levels. J Physiol 289:33–53. CrossRef Medline

Smith SL, Häusser M (2010) Parallel processing of visual space by neighboring neurons in mouse visual cortex. Nat Neurosci 13:1144–1149. CrossRef Medline

Stosiek C, Garaschuk O, Holthoff K, Konnerth A (2003) In vivo two-photon calcium imaging of neuronal networks. Proc Natl Acad Sci U S A 100:7319–7324. CrossRef Medline

Sundberg KA, Mitchell JF, Reynolds JH (2009) Spatial attention modulates center-surround interactions in macaque visual area v4. Neuron 61:952–963. CrossRef Medline

Tahvildari B, Wölfel M, Duque A, McCormick DA (2012) Selective functional interactions between excitatory and inhibitory cortical neurons and differential contribution to persistent activity of the slow oscillation. J Neurosci 32:12165–12179. CrossRef Medline

Thévenaz P, Ruttimann UE, Unser M (1998) A pyramid approach to subpixel registration based on intensity. IEEE Trans Image Process 7:27–41. CrossRef Medline

Vidyasagar TR, Sigüenza JA (1985) Relationship between orientation tuning and spatial frequency in neurones of cat area 17. Exp Brain Res 57:628–631. Medline

Vreysen S, Zhang B, Chino YM, Arckens L, Van den Bergh G (2012) Dynamics of spatial frequency tuning in mouse visual cortex. J Neurophysiol 107:2937–2949. CrossRef Medline

Wang J, Caspary D, Salvi RJ (2000) GABA-A antagonist causes dramatic expansion of tuning in primary auditory cortex. Neuroreport 11:1137–1140. CrossRef Medline

Webster MA, De Valois RL (1985) Relationship between spatial-frequency and orientation tuning of striate-cortex cells. J Opt Soc Am A 2:1124–1132. CrossRef Medline

Wertz A, Trenholm S, Yonehara K, Hillier D, Raics Z, Leinweber M, Szalay G, Ghanem A, Keller G, Rózsa B, Conzelmann KK, Roska B (2015) PRESYNAPTIC NETWORKS. Single-cell-initiated monosynaptic tracing reveals layer-specific cortical network modules. Science 349:70–74. CrossRef Medline

Wilson NR, Runyan CA, Wang FL, Sur M (2012) Division and subtraction by distinct cortical inhibitory networks in vivo. Nature 488:343–348. CrossRef Medline

Womelsdorf T, Anton-Erxleben K, Pieper F, Treue S (2006) Dynamic shifts of visual receptive fields in cortical area MT by spatial attention. Nat Neurosci 9:1156–1160. CrossRef Medline

Xu X, Roby KD, Callaway EM (2010) Immunochemical characterization of inhibitory mouse cortical neurons: three chemically distinct classes of inhibitory cells. J Comp Neurol 518:389–404. CrossRef Medline

Yeshurun Y, Carrasco M (1998) Attention improves or impairs visual performance by enhancing spatial resolution. Nature 396:72–75. CrossRef Medline

Yilmaz M, Meister M (2013) Rapid innate defensive responses of mice to looming visual stimuli. Curr Biol 23:2011–2015. CrossRef Medline

Yizhar O, Fenno LE, Prigge M, Schneider F, Davidson TJ, O'Shea DJ, Sohal VS, Goshen I, Finkelstein J, Paz JT, Stehfest K, Fudim R, Ramakrishnan C, Huguenard JR, Hegemann P, Deisseroth K (2011) Neocortical excitation/inhibition balance in information processing and social dysfunction. Nature 477:171–178. CrossRef Medline

Zhang S, Xu M, Kamigaki T, Hoang Do JP, Chang WC, Jenvay S, Miyamichi K, Luo L, Dan Y (2014) Selective attention: long-range and local circuits for top-down modulation of visual cortex processing. Science 345:660–665. CrossRef Medline

Zhu W, Xing D, Shelley M, Shapley R (2010) Correlation between spatial frequency and orientation selectivity in V1 cortex: implications of a network model. Vision Res 50:2261–2273. CrossRef Medline